Journal of Applied Physics

RESEARCH ARTICLE | MAY 12 2023

Explosive crystallization of amorphous germanium-tin films by irradiation with a 3-keV electron beam

R. Nakamura ✉ ; M. Miyamoto ; M. Ishimaru

Journal of Applied Physics 133, 185304 (2023)
https://doi.org/10.1063/5.0147022

AIP Publishing

Journal of Applied Physics ARTICLE scitation.org/journal/jap

Explosive crystallization of amorphous germanium-tin films by irradiation with a 3-keV electron beam

Cite as: J. Appl. Phys. **133**, 185304 (2023); doi: 10.1063/5.0147022
Submitted: 18 February 2023 · Accepted: 30 April 2023 ·
Published Online: 12 May 2023

R. Nakamura,[1,a),b)] M. Miyamoto,[1] and M. Ishimaru[2]

AFFILIATIONS

[1]Department of Materials Science, Graduate School of Engineering, Osaka Prefecture University, Gakuen-cho 1-1, Naka-ku, Sakai 599-8531, Japan
[2]Department of Materials Science and Engineering, Kyushu Institute of Technology, Tobata, Kitakyushu, Fukuoka 804-8550, Japan

[b)]**Author to whom correspondence should be addressed:** nakamura.r@mat.usp.ac.jp
[a)]**Present address:** Department of Materials Science, School of Engineering, The University of Shiga Prefecture, Hassaka-cho 2500, Hikone 522-8533, Japan.

ABSTRACT

Much effort has been expended to obtain thin films of metastable solid solutions of germanium (Ge) that contain as high tin (Sn) content as possible because of their excellent electronic and optoelectronic properties. On the basis of our previous study on amorphous Ge, we demonstrated in this study that irradiation of substrate-free films of amorphous $Ge_{100-x}Sn_x$ ($x = 8$, 11, and 19 at. %) with a low-energy electron beam of 3 keV at ambient temperature can induce instantaneous wide-area crystallization (explosive crystallization). Characteristic spiral crystal growth associated with explosive crystallization occurred with areas exceeding 50 μm in diameter around a scanned area of the electron beam of $8 \times 8\,\mu m^2$. As a result, solid solutions of GeSn with Sn concentration up to 19 at. % were obtained with the suppression of precipitation of β-Sn. The region of explosive crystallization reduced in size with increasing Sn content. In addition, thermal analyses revealed that the heat released during crystallization of amorphous GeSn films decreased with increasing Sn content. This relationship indicates that the heat release at the growth front plays a key role in the propagation of explosive crystallization of a-GeSn.

I. INTRODUCTION

Thin films of polycrystalline germanium (Ge) that contain tin (Sn) have attracted interest for use in electronic devices because they have higher carrier mobilities than Ge and in optoelectronic applications owing to their direct bandgap structure.[1,2] Much effort has been devoted to obtain solid solutions of Ge with as high Sn content as possible to achieve the required properties for such applications. The target Sn concentration is theoretically predicted to be 6–10 at. %,[3–5] at which the electronic band structure changes from indirect to direct. To date, metastable solid solutions of GeSn up to 20 at. % Sn have been experimentally obtained by various techniques,[6–16] against the intrinsically low solubility, at most 1 at. %, of Sn in Ge.[17]

One of the processes used to obtain polycrystalline films of Ge and its alloys is crystallization of amorphous films. In this process, amorphous films are deposited on glass substrates and then crystallized by annealing processes, such as conventional furnace-heating,[18,19] laser annealing,[20–22] or flash-lamp annealing.[23,24] In the production of GeSn films, a low-temperature process is essential for two reasons: to reduce thermal damage of insulating substrates and to realize a phase transition from amorphous to metastable solid solution without precipitation of β-Sn.

Explosive crystallization was first reported for amorphous Ge (a-Ge) by Takamori *et al.*[25] Explosive crystallization is rapid and covers a wide area. It is triggered by instantaneous processes, such as mechanical stimulation,[25] laser irradiation,[26–28] electron-beam heating,[29] and flash-lamp annealing.[30] Recently, we demonstrated that explosive crystallization of a-Ge could be induced by irradiation of an electron beam at low energies below 20 keV at ambient

temperature in a scanning electron microscope (SEM).[31] This occurred most efficiently at 3 keV, at which the threshold electron flux required for explosive crystallization was the lowest, which meant that there was a negligible temperature rise of the film due to beam heating. A region exceeding 100 μm in diameter crystallized instantaneously by scanning an electron beam over an area of $8 \times 8\ \mu m^2$ in substrate-free films. Thus, a 3-keV electron beam can induce crystallization of a-Ge with low thermal budget and energy consumption. We expect that this would also be effective for inducing crystallization of a-Ge containing Sn.

In this study, we used a 3-keV electron beam to induce explosive crystallization of amorphous GeSn (a-GeSn) with Sn concentrations up to 23 at. %. We found that explosive crystallization can be induced to form solid solutions of GeSn of up to 19 at. % Sn, in which the precipitation of β-Sn was suppressed to a considerable degree. The mechanism of explosive crystallization in a-GeSn is discussed based on two analyses: the structural analysis of a-GeSn in terms of pair-distribution function and the thermal analysis of heat release during crystallization of a-GeSn.

II. EXPERIMENTAL PROCEDURE

A. Sample preparation

Thin films of amorphous GeSn (a-GeSn) of 40-nm thickness were prepared by radio-frequency (RF) sputtering at a base pressure below 5×10^{-5} Pa. Polycrystalline Ge with a purity of 99.99% and a diameter of 101.6 mm was used as the base target. Sheets of Sn with dimensions of $5 \times 5 \times 1\ mm^3$ and a purity of 99.99% were placed on the Ge target to obtain amorphous films at concentrations of 8–23 at. % Sn by adjusting the areal ratio of Sn to Ge.[16] Cleaved crystals of sodium chloride (NaCl) with dimensions of approximately $4 \times 4 \times 2\ mm^3$ were used as the substrate. Thin films of 40-nm thickness were deposited on the clean surface of the substrates, which were kept at ambient temperature. Deposition was conducted by sputtering composite targets under an RF output power of 50 W and in a stream of argon of 0.7–0.8 Pa. The films on the substrates were placed in distilled water, and the floating films were recovered on copper (Cu) grids with a hole size of $100 \times 100\ \mu m^2$.

The concentration of Sn of the prepared films was measured to be 8.4, 11.4, 18.8, and 23.0 at. % Sn using a transmission electron microscope (TEM) (JEOL, JEM-3000F) with an energy-dispersive x-ray spectrometer. We refer to these samples as 8Sn, 11Sn, 19Sn, and 23Sn.

B. Electron irradiation and observation

The samples were irradiated with a 3-keV electron beam at ambient temperature in an electron probe microanalyzer (EPMA) (JEOL, JXA-8530F). The current of the incident electron-beam was monitored using a Faraday cage with a size of 62.2 mm^2. The diameter of the focused electron beam was less than 1 μm. We set the scanning area of the electron beam to be $8 \times 8\ \mu m^2$, which was the smallest irradiation area for inducing explosive crystallization of a-Ge.[31]

The microstructure of the irradiated region was observed *in situ* using the SEM of EPMA and also *ex situ* using a TEM (JEOL, JEM-2000FX) operated at 200 kV. In addition, elemental-mapping images were obtained using a scanning TEM (JEOL, JEM-F200) with an energy-dispersive x-ray spectrometer.

C. Pair-distribution function analysis

The electron-scattering patterns of a-GeSn films were obtained using a TEM (JEOL-3000F) operated at 300 keV. The beam diameter was approximately 300 nm and the scattering patterns were recorded on an imaging plate (Eu^{2+}-doped BaFBr). From intensity profiles scanned using an imaging plate processor (DITABIS Micron Vario), the reduced interference functions, $F(Q)$, were extracted as a function of the magnitude of the scattering vector Q; Q is defined as $4\pi\sin\theta/\lambda$, where θ and λ are the scattering angle and the electron wavelength, respectively. Pair-distribution functions were obtained by Fourier transforming $F(Q)$. The details are described in Ref. 32

D. Differential scanning calorimetry analysis

A thin plate of borosilicate glass (D263) with a density of $2.5\ g\ cm^{-3}$ and dimensions of $50 \times 50 \times 0.05\ mm^3$ was used as the substrate. A thin film of a-Ge and a-GeSn of 200-nm thickness was deposited on both sides of the substrate by sputtering targets under same conditions as described above. Pieces of the crushed glass substrate (which had a total film thickness of 400 nm) were placed in a crucible composed of inner alumina and outer platinum layers. The total mass of the pieces was set to be approximately 40 mg; the mass of the a-Ge or a-GeSn film was measured to be 0.6–0.7 mg from the difference in mass between the substrate before and after deposition. The furnace of a differential scanning calorimeter (DSC) (Netzch, DSC404F3) was evacuated by a rotary pump, and then argon gas (99.999%) was set to flow at a rate of $50\ ml\ min^{-1}$. The DSC profile was measured in the temperature range of 313–870 K at heating and cooling rates of 2, 5, and 10 $K\ min^{-1}$.

III. RESULTS AND DISCUSSION

A. Explosive crystallization of amorphous GeSn thin films

1. SEM images of irradiated amorphous films

Figures 1(a)–1(d) show the example of SEM images of regions of a-GeSn samples irradiated at 3 keV in the EPMA for (a) 8Sn, (b) 11Sn, (c) 19Sn, and (d) 23Sn, respectively. The electron flux was 3.0×10^{15}, 3.0×10^{15}, 2.0×10^{15}, and $1.4 \times 10^{15}\ m^{-2}\ s^{-1}$, respectively. The dotted squares and circles in Fig. 1(c) indicate the scanned area of the electron beam ($8 \times 8\ \mu m^2$) and the resultant crystallization area where explosive crystallization occurred, respectively. The labels *a* and *c* refer to amorphous and crystalline regions, respectively, and the dotted circles are roughly drawn to guide for eyes as a visual guide to indicate the boundary. In Figs. 1(a)–1(c), distinctive circular patterns can be seen over a wide diameter of 60–100 μm. These patterns are similar to that observed in a-Ge in our previous report[31] and are also a typical feature of explosive crystallization,[25–30] which occurs instantaneously when a-Ge is subjected to stimulation. By contrast, for 23Sn [Fig. 1(d)], no pattern can be seen and there is a slight change in contrast in

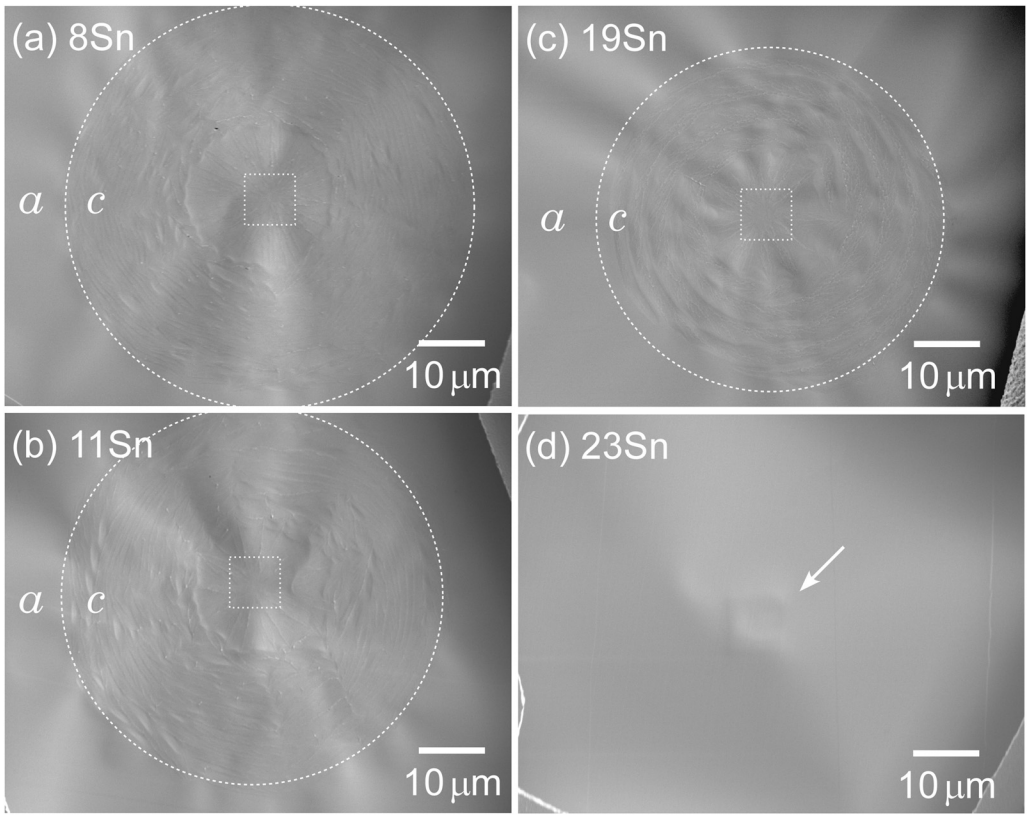

FIG. 1. Scanning electron microscope (SEM) images of crystallized regions in amorphous GeSn films by irradiation of a 3-keV electron beam: the concentration of Sn is (a) 8% (8Sn), (b) 11% (11Sn), (c) 19% (19Sn), and (d) 23% (23Sn). Lines are drawn for guide for eyes: the dotted squares indicate the scanned area of the electron beam, $8 \times 8\,\mu m^2$, and the dotted circles indicate the boundary between the explosively crystallized region, *c*, and amorphous region, *a*. The arrow in (d) indicates a trace by electron irradiation of $8 \times 8\,\mu m^2$.

the $8 \times 8\,\mu m^2$ scanned area of the electron beam, as indicated by the arrow. No explosive crystallization occurred in a-GeSn of 23 at. % Sn, but nano-sized crystalline grains homogeneously appeared in the scanned region. We discuss this further in Sec. III A 2 in relation to TEM observations.

The extent of explosive crystallization that occurred is noteworthy. The addition of Sn to a-Ge resulted in a decrease in the diameter of the areas formed via explosive crystallization: 100 μm for 0Sn,[31] 80 μm for11Sn, and 60 μm for 19Sn. The effect is discussed in Sec. III C in terms of heat released during crystallization as evaluated by the thermal analysis.

We observed explosive crystallization in a-GeSn at Sn concentrations up to 19 at. % Sn under irradiation of electron beams of 2–20 keV. We examined explosive crystallization by irradiating a pristine area with an electron beam of a set current. By raising the beam current (electron flux) in steps of 5 nA ($5.0 \times 10^{14}\,m^{-2}\,s^{-1}$), we determined the threshold beam current (electron flux) at which the pattern of explosive crystallization pattern appeared. Therefore, the error bar covers the lower limit of the step. Figure 2 shows the relationship between the electron energy and threshold electron flux for inducing explosive crystallization of 11Sn. The previously reported data for a-Ge (0Sn) are also shown together. The threshold electron flux for 11Sn was approximately 50% that for 0Sn; thus, the addition of Sn facilitates the induction of explosive crystallization. This tendency is consistent with previously reported observations of crystallization of a-GeSn in a 75-keV electron beam of a TEM.[33] By contrast, we reported that the addition of Si to a-Ge increases the electron flux needed for crystallization.[34] The addition of Sn to a-Ge decreases the bond strength, whereas the addition of Si increases it.[35] Therefore, we suggest that the bond strength is associated with the electron flux needed for crystallization. The threshold flux for 11Sn reached a minimum value at 3 keV, as is the case for 0Sn. This can be explained in terms of the electronic excitation mechanism; the excitation of the *K* shell of Ge by the electron beam is highly efficient at around 3 keV, where the cross section for ionization is close to its maximum value.[31]

2. Crystallization microstructure

Figures 3(a)–3(c) show typical examples of the microstructure of explosive crystallization region of 11Sn, 19Sn, and 23Sn, respectively, by irradiation at 3 keV. The image X is the overall

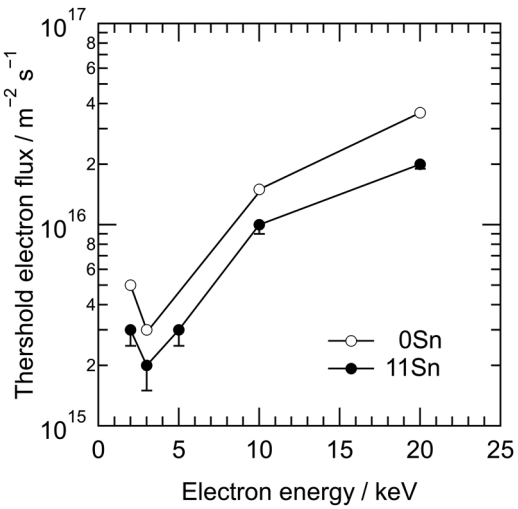

FIG. 2. The relationship between the electron energy and threshold electron flux required to induce explosive crystallization of a-GeSn (11Sn). Our previous data for a-Ge (0Sn)[31] are shown for comparison. Lines between points are drawn for guide for eyes.

crystallized region and the dotted square indicates the $8 \times 8\,\mu m^2$ region irradiated by the electron beam. Images X1 and X2 correspond to magnified TEM views of central region 1 and outer region 2 in X, respectively. For 11Sn [Fig. 3(a)] and 19Sn [Fig. 3(b)], crystallization occurred radially at region 1 and spirally at region 2. These microstructures are similar to those reported previously for a-Ge (0Sn).[25–31] By contrast, in 23Sn [Fig. 3(c)], nano-sized crystalline grains homogeneously appeared at regions 1 and 2, within almost the same region of the scanned area of the electron beam.

Y1 and Y2 in Figs. 3(a)–3(c) show selected-area electron-diffraction patterns taken from regions 1 (in image X1) and 2 (image X2), respectively. The major Debye–Scherrer rings were identified as 111, 220, and 311 of the diamond cubic structure, respectively. In addition, weak and broad rings appeared continuously outside the 111 ring of the diamond cubic structure in Y1 and Y2 of 19Sn and Y1 of 23Sn. These rings split in Y1 of 23Sn but overlap in Y1 and Y2 of 19Sn, and are attributable to diffractions of 200 and 101 of β-Sn, as indicated by the italic text. In the converted intensity profiles of Y1 and Y2 (Fig. S1 in the supplementary material), the weak rings of β-Sn can be seen as weak peaks. In 11Sn, a faint diffraction spot of β-Sn appeared in region 1 (image Y1) but not in region 2 (image Y2). In region 1, which was subject to direct irradiation of the electron beam, a small amount of β-Sn precipitated in 11Sn.

Figures 4(a)–4(c) show the elemental-mapping images of the crystallized regions of 11Sn, 19Sn, and 23Sn, respectively; peripheral region 2 of 11Sn and 19Sn and central region 1 of 23Sn are shown. In 23Sn, regions of dark and bright contrast of Ge Kα and Sn Lα, respectively, are clearly distributed, indicating that there was substantial precipitation of β-Sn with 100-nm diameter in the crystallized region. Small regions of bright contrast of Sn Lα can be seen in 11Sn and 19Sn, but no regions of dark contrast of Ge Kα can be recognized in the samples. Therefore, the contrast is probably not due to the intensity of characteristic x ray but to fluctuations in film thickness. The electron-diffraction patterns of 19Sn [Fig. 3(b), images Y1 and Y2] indicate the appearance of β-Sn, but the elemental mapping does not. These results suggest that β-Sn precipitates are extremely small.

In summary, as a result of explosive crystallization of a-GeSn with up to 19 at. % Sn, solid solutions with a diamond cubic structure form preferentially. Notably, the precipitation of β-Sn was strongly suppressed in 11Sn. Because of the precipitation of β-Sn, the solid solutions contained a lower concentration of Sn than the initial concentration of amorphous states. By contrast, for a-GeSn of 23 at. %, nano-sized crystalline grains homogeneously appeared with notable precipitation of β-Sn. Explosive crystallization in a-GeSn competes with the precipitation of β-Sn.

B. Pair-distribution function analysis of amorphous GeSn

Figures 5(a) and 5(b) show the reduced-interference function $F(Q)$ and pair-distribution function, $g(r)$, respectively, of amorphous 11Sn, 19Sn, and 23Sn with those of a-Ge (0Sn) as a reference. The undulations of $F(Q)$ of all samples, including 0Sn, are similar over the scattering vector $Q = 250\ nm^{-1}$, whereas the amplitude decreases with increasing Sn content. Studies have empirically shown that the damping of $F(Q)$ of metallic matters continues to smaller scattering vectors than that of non-metallic matters.[36,37] Thus, the decrease in the amplitude of $F(Q)$ upon addition of Sn is attributable to the increase in Sn–Sn metallic bonds.[16] Moreover, the wavelength of $F(Q)$ of 23Sn was shorter than those of other samples.

In pair-distribution functions of all samples [Fig. 5(b)], the intensity peaks are located at the interatomic distance of Ge–Ge bonds around 0.25, 0.40, and 0.61 nm. Figure 5(b′) is an enlarged view of the first peak, showing that the intensities at 0.25 nm decrease and broaden with increasing Sn content. Notably, the peak position of 23Sn is located at a greater distance than that of other samples. The shoulder peaks, which are indicated by arrows, are due to superposition of correlation peaks of Ge–Sn bonds of 0.26-nm length and Sn–Sn bonds of 0.28-nm length. The shoulder peaks of 11Sn and 19Sn are similar, whereas that of 23Sn is higher. These properties suggest that the amorphous structure changes at Sn concentrations over 20 at. % because of the increase in Sn-related bonds.

As discussed in Sec. III A, the boundary concentration of Sn, below which explosive crystallization occurs upon electron-beam irradiation at 3 keV, is between 19 and 23 at. %. A notable decrease in the number of Ge–Ge bonds and the increase in the number of Ge–Sn and Sn–Sn bonds can be inferred from $g(r)$ of 19Sn and 23Sn, which is a crucial factor in changing the crystallization mode. We propose that explosive crystallization is actuated by medium-range ordered clusters in the sputter-deposited a-Ge, which behave as nuclei[38] and by a fluid-interface layer of a liquid-like state, which facilitates extremely rapid crystal growth.[27,28,38] An excessive number of Sn-related bonds in amorphous GeSn matrices may

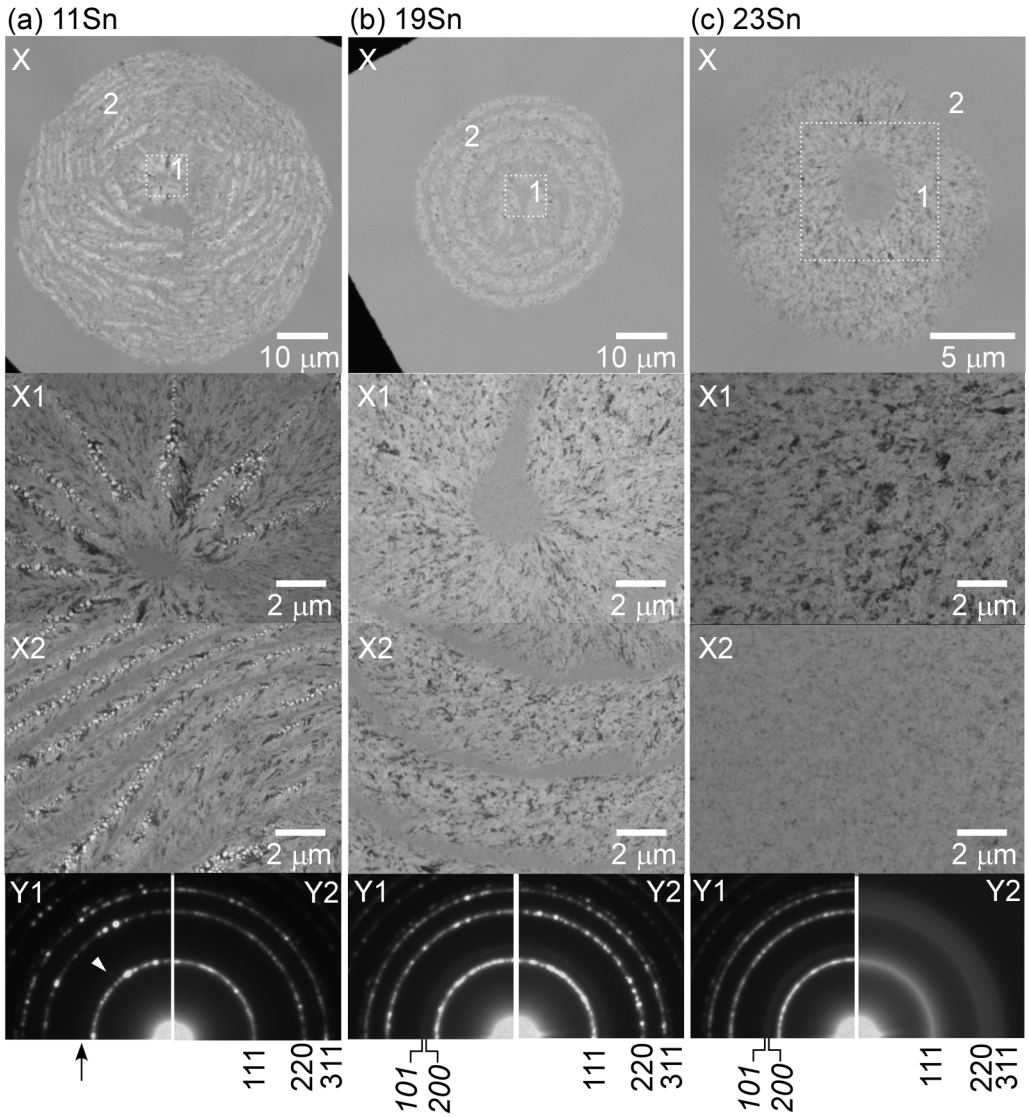

FIG. 3. TEM images of crystallized regions of (a) 11Sn, (b) 19Sn, and (c) 23Sn. Images X correspond to the whole region of crystallization in the amorphous films, and X1 and X2 correspond to the magnified views of the region 1 and region 2. The dotted squares indicate the scanned area of the electron beam, $8 \times 8\,\mu m^2$. Y1 and Y2 show corresponding electron-diffraction patterns of X1 and X2. Numbers in roman and italic in Y1 and Y2 mean the plane indices of the diamond cubic structure of solid solution of GeSn and β-Sn, respectively. The arrow in Y1 of (a) is the weak spot of 200 or 101 of β-Sn.

alter the conditions of explosive crystallization in a-Ge. For example, they may destabilize medium-range ordered clusters and/or the fluid layer and, therefore, may impede the initial process of atomic arrangement for the actuation of explosive crystallization.

C. Heat release by crystallization of amorphous GeSn

As mentioned in Sec. III A 1, the extent of explosive crystallization decreased with increasing Sn content. A unique feature of explosive crystallization is the spiral motion of the growing interfacial layer, at which heat release by transition from amorphous to crystalline phases can assist continuous growth.[27,28,39–42] To determine the effect of Sn on the extent of explosive crystallization, the heat released from crystallization of a-Ge and a-GeSn was evaluated using DSC.

Figure 6 shows the partial DSC profiles of a-Ge (0Sn) and a-GeSn (8Sn, 11Sn, and 19Sn) at a heating rate of $5\,K\,min^{-1}$ (see Fig. S2 in the supplementary material for entire profiles from 40 to 580 °C). The signal intensity decreased above 530 °C, which is the glass transition temperature of the substrate. A single, exothermic

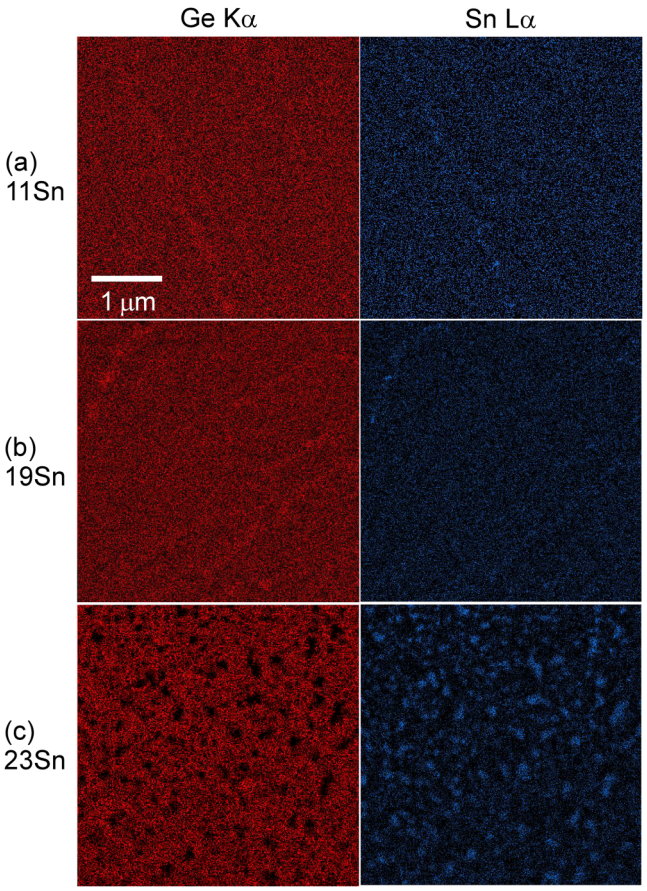

FIG. 4. Elemental-mapping images of Ge (left hand) and Sn (right hand) in the crystallized regions of (a) 11Sn, (b) 19Sn, and (c) 23Sn. The scale bar in the upper left image is common. Bright contrast corresponds to high intensity of the characteristic x ray.

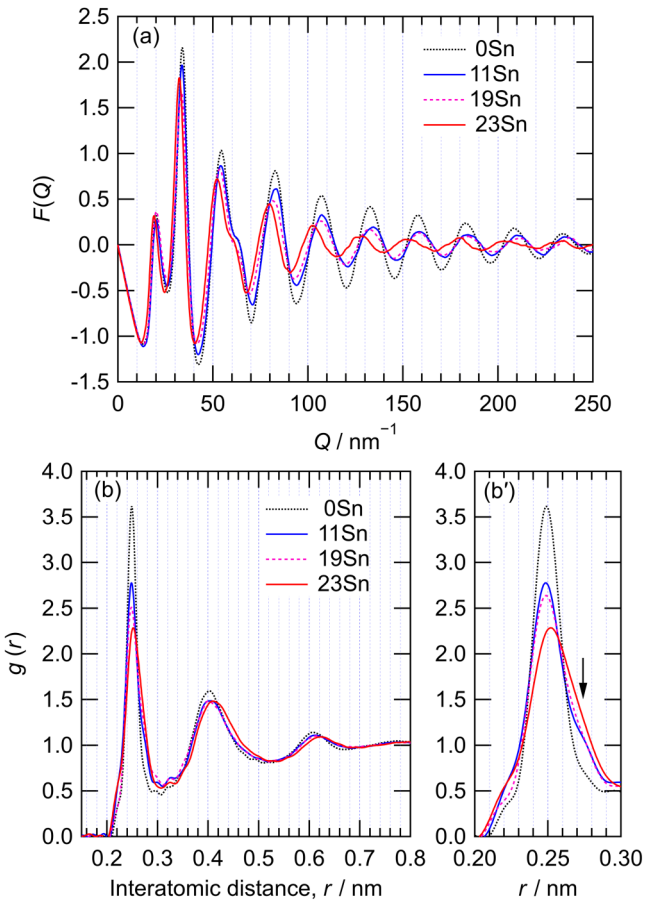

FIG. 5. (a) Reduced interference function, $F(Q)$, of a-GeSn analyzed by transmission electron microscopy and (b) pair-distribution function, $g(r)$, as the Fourier transform of $F(Q)$. (b′) An enlarged part of the first peak of $g(r)$.

peak appeared at approximately 520 and 500 °C in 0Sn and 8Sn, respectively, as shown by arrows. By contrast, double exothermic peaks appeared around 460 °C in 11Sn. In 19Sn, a single, exothermic peak appeared broadly at around 400 °C. The weak peak at approximately 430 °C was not due to a thermal event of the sample but to an extrinsic deviation from the base line.

According to *in situ* TEM observations made under isochronal annealing, the crystallization temperature of 0Sn is 500 °C,[43] and those of 8Sn, 11Sn, and 20Sn are 380, 320, and 280 °C, respectively.[16] The crystallization temperatures observed using DSC were higher than those obtained using TEM. This is reasonable because the samples subjected to isochronal annealing in TEM underwent greater heating than those subjected to continuous heating in DSC; the temperature was increased in a stepwise manner in TEM, and the specimens were kept for at least 10 min at each temperature to take images and diffraction patterns without thermal drift.[16,43] A common feature of DSC and TEM studies is that the crystallization temperature decreases with increasing Sn content.

Notably, two separate exothermic peaks were observed in 11Sn at approximately 450 and 470 °C. This result is because the amorphous GeSn first crystallized to the solid solution at lower temperatures and subsequently β-Sn precipitated at higher temperatures, as shown in TEM images (see Fig. S3 in the supplementary material). The exothermic peak was a single peak for 8Sn and 19Sn; however, β-Sn precipitated to a small extent in 8Sn and to a large extent in 19Sn. The signal for precipitation was likely too weak to be detected for 8Sn, and crystallization and precipitation were not separate but occurred simultaneously in 19Sn under heating.

The heat release during crystallization of 0Sn, 8Sn, and 11Sn was evaluated from the area of exothermic peaks to be 8.4 ± 0.5, 3.2 ± 0.1, and 1.2 ± 0.2 kJ mol^{-1}, respectively. These are average values of peak areas observed at heating rates of 2, 5, and 10 K min^{-1}, and the experimental error is the standard deviation. The value of 0Sn (a-Ge), 8.4 kJ mol^{-1}, is comparable to the literature data, 11–16 kJ mol^{-1}.[44–49] The addition of Sn to a-Ge lowers the heat release during crystallization. Heat release at the interface

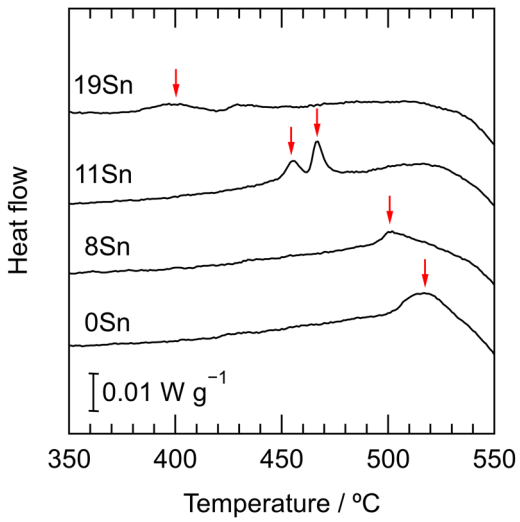

FIG. 6. DSC profiles of a-Ge (0Sn) and a-GeSn (8Sn, 11Sn, and 19Sn) at a heating rate of 5 K min^{-1}. Upward is an exothermic direction. The entire profiles are shown in Fig. 1 in the supplementary material.

between amorphous and crystalline phases is generally accepted to assist the spiral growth of explosive crystallization. Crystal growth during explosive crystallization of a-GeSn would be less continuous than that of a-Ge because of the weaker contribution of heat release at the growth front.

The temperature rise, ΔT, upon electron-beam irradiation can be estimated using the following equation:[50,51]

$$\Delta T = W[1 + 2\ln(R/r)]/(4\pi lk), \quad (1)$$

where R is the radius of the film within a hole of a supporting Cu grid (50 μm), r is the radius of the beam (0.5 μm), l is the specimen thickness (40 nm), and k is the thermal conductivity (0.5 W m^{-1} K^{-1} for a-Ge).[52] The total absorbed power, W, is expressed as $W = \epsilon VI$, where ϵ is the fraction of energy absorbed (usually 0.01),[51] V is the acceleration voltage (3 kV), and I is the beam current (maximum value of 30 nA). ΔT was estimated to be no greater than 40 K, being much lower than the thermal crystallization temperature, which was determined from DSC to be above 650 K. However, β-Sn precipitated in the region irradiated by the electron beam, suggesting that the instantaneous temperature rise due to the electron beam may be higher than the estimated value. Heat release during crystallization and energy transfer from the electron beam must both be considered to enable understanding of the mechanism of explosive crystallization of a-GeSn and to suppress the precipitation of β-Sn.

IV. SUMMARY

We demonstrated that irradiating substrate-free films of amorphous GeSn containing up to 19 at. % Sn with a 3-keV electron beam at ambient temperature induces explosive crystallization. As a result, solid solutions were athermally and efficiently produced with the precipitation of β-Sn suppressed. However, above 20 at. % Sn, the precipitation of β-Sn rather than explosive crystallization preferentially occurred because Sn-related bonds in the amorphous matrix impeded rapid crystal growth. Further studies on explosive crystallization of a-Ge and a-GeSn films deposited on various substrates are underway to show the potential of this technique.

SUPPLEMENTALY MATERIALS

See the supplementary material for the following: Fig. S1 for converted intensity profiles of selected area diffraction patterns of crystallized regions shown in Fig. 3. See Fig. S2 for entire profiles of DSC curves of four samples, corresponding to Fig. 6. See Fig. S3 for TEM images of 11Sn subjected to annealing in the DSC furnace up to the end temperature of first and second exothermic peaks.

ACKNOWLEDGMENTS

This work was financially supported by the Murata Science Foundation (No. M20-074) and Japan Society for the Promotion of Science (JSPS) KAKENHI (Grant No. 22H01815). M.I. would like to express his gratitude to the Izumi Science and Technology Foundation (No. 2022-J-026).

AUTHOR DECLARATIONS

Conflict of Interest

The authors have no conflicts to disclose.

Author Contributions

R. Nakamura: Conceptualization (lead); Data curation (lead); Formal analysis (lead); Funding acquisition (lead); Investigation (equal); Methodology (lead); Project administration (lead); Resources (equal); Supervision (lead); Validation (equal); Visualization (lead); Writing – original draft (lead); Writing – review & editing (lead). **M. Miyamoto:** Formal analysis (equal); Investigation (lead); Methodology (equal). **M. Ishimaru:** Conceptualization (supporting); Data curation (equal); Formal analysis (equal); Investigation (supporting); Methodology (supporting); Supervision (equal); Validation (supporting); Writing – review & editing (supporting).

DATA AVAILABILITY

The data that support the findings of this study are available within the article.

REFERENCES

[1]S. Zaima, O. Nakatsuka, N. Taoka, M. Kurosawa, W. Takeuchi, and M. Sakashita, Sci. Technol. Adv. Mater. **16**, 043502 (2015).
[2]N. Uchida, T. Maeda, R. R. Lieten, S. Okajima, Y. Ohishi, R. Takase, M. Ishimaru, and J.-P. Locquet, Appl. Phys. Lett. **107**, 232105 (2015).
[3]K. Alberi, J. Blacksberg, L. D. Bell, S. Nikzad, K. M. Yu, O. D. Dubon, and W. Walukiewicz, Phys. Rev. B **77**, 073202 (2008).
[4]R. Chen, H. Lin, Y. Huo, C. Hitzman, T. I. Kamins, and J. S. Harris, Appl. Phys. Lett. **99**, 181125 (2011).

[5]W. Du, S. A. Ghetmiri, B. R. Conley, A. Mosleh, A. Nazzal, R. A. Soref, G. Sun, J. Tolle, J. Margetis, H. A.1 Naseem, and S.-Q. Yu, Appl. Phys. Lett. **105**, 051104 (2014).
[6]M. Bauer, J. Taraci, J. Tolle, A. V. G. Chizmeshya, S. Zollner, D. J. Smith, J. Menendez, C. Hu, and J. Kouvetakis, Appl. Phys. Lett. **81**, 2992–2994 (2002).
[7]M. Nakamura, Y. Shimura, S. Takeuchi, O. Nakatsuka, and S. Zaima, Thin Solid Films **520**, 3201–3205 (2012).
[8]M. Kurosawa, N. Taoka, M. Sakashita, O. Nakatsuka, M. Miyao, and S. Zaima, Appl. Phys. Lett. **103**, 101904 (2013).
[9]R. R. Lieten, J. W. Seo, S. Decoster, A. Vantomme, S. Peters, K. C. Bustillo, E. E. Haller, M. Menghini, and J.-P. Locquet, Appl. Phys. Lett. **102**, 052106 (2013).
[10]H. Chikita, R. Matsumura, Y. Kai, T. Sadoh, and M. Miyao, Appl. Phys. Lett. **105**, 202112 (2014).
[11]K. Toko, N. Oya, N. Saitoh, N. Yoshizawa, and T. Suemasu, Appl. Phys. Lett. **106**, 082109 (2015).
[12]R. Matsumura, H. Chikita, Y. Kai, T. Sadoh, H. Ikenoue, and M. Miyao, Appl. Phys. Lett. **107**, 262106 (2015).
[13]M. Kim, W. Fan, J.-H. Seo, N. Cho, S.-C. Liu, D. Geng, Y. Liu, S. Gong, X. Wang, W. Zhou, and Z. Ma, Appl. Phys. Express **8**, 061301 (2015).
[14]R. Takase, M. Ishimaru, N. Uchida, T. Maeda, K. Sato, R. R. Lieten, and J.-P. Locquet, J. Appl. Phys. **120**, 245304 (2016).
[15]K. Moto, N. Saitoh, N. Yoshizawa, T. Suemasu, and K. Toko, Appl. Phys. Lett. **114**, 112110 (2019).
[16]M. Higashiyama, M. Ishimaru, M. Okugawa, and R. Nakamura, J. Appl. Phys. **125**, 175703 (2019).
[17]R. W. Olesinski and G. J. Abbaschian, Bull. Alloy Phase Diagrams **5**, 265 (1984).
[18]K. Toko, I. Nakao, T. Sadoh, T. Noguchi, and M. Miyao, Solid-State Electron. **53**, 1159 (2009).
[19]S. Kabuyanagi, T. Nishimura, K. Nagashio, and A. Toriumi, Thin Solid Films **557**, 334 (2014).
[20]H. Watakabe, T. Sameshima, H. Kanno, and M. Miyao, Thin Solid Films **508**, 315 (2006).
[21]W. Yeh, H. Chen, H. Huang, C. Hsiao, and J. Jeng, Appl. Phys. Lett. **93**, 094103 (2008).
[22]K. Sakaike, S. Higashi, H. Murakami, and S. Miyazaki, Thin Solid Films **516**, 3595 (2008).
[23]K. Usuda, Y. Kamata, Y. Kamimuta, T. Mori, M. Koike, and T. Tezuka, Appl. Phys. Express **7**, 056501 (2014).
[24]N. Matsuo, N. Yoshioka, and A. Heya, Jpn. J. Appl. Phys. **56**, 085505 (2017).
[25]T. Takamori, R. Messier, and R. Roy, Appl. Phys. Lett. **20**, 201 (1972).
[26]H. J. Leamy, W. L. Brown, G. K. Celler, G. Foti, G. H. Gilmer, and J. C. C. Fan, Appl. Phys. Lett. **38**, 137 (1981).
[27]L. Nikolova, M. J. Stern, J. M. MacLeod, B. W. Reed, H. Ibrahim, G. H. Campbell, F. Rosei, T. LaGrange, and B. J. Siwick, J. Appl. Phys. **116**, 093512 (2014).
[28]G. Egan, T. T. Rahn, A. J. Rise, H.-Y. Cheng, S. Raoux, G. H. Campbell, and M. K. Santala, J. Appl. Phys. **26**, 105110 (2019).
[29]J. R. Parsons and C. W. Hoelke, Philos. Mag. A **50**, 329 (1985).
[30]K. Ohdaira and H. Matsumura, Thin Solid Films **524**, 161 (2012).
[31]R. Nakamura, A. Matsumoto, and M. Ishimaru, J. Appl. Phys. **129**, 215301 (2021).
[32]M. Ishimaru, Nucl. Instrum. Methods Phys. Res. Sect. B **250**, 309 (2006).
[33]T. Kimura, M. Ishimaru, M. Okugawa, R. Nakamura, and H. Yasuda, Jpn J. Appl. Phys. **56**, 100307 (2017).
[34]M. Okugawa, R. Nakamura, H. Numakura, M. Ishimaru, and H. Yasuda, J. Appl. Phys. **128**, 015303 (2020).
[35]A. S. Vasin, F. Oliveira, M. F. Cerqueira, J. Schulze, and M. I. Vasilevskiy, J. Appl. Phys. **124**, 035105 (2018).
[36]T. Fukunaga, K. Itoh, T. Otomo, K. Mori, M. Sugiyama, H. Kato, M. Hasegawa, A. Hirata, Y. Hirotsu, and A. C. Hannon, Intermetallics **14**, 893 (2006).
[37]A. Hirata, Y. Hirotsu, K. Amiya, and A. Inoue, Phys. Rev. B **79**, 020205 (2009).
[38]M. Okugawa, R. Nakamura, H. Numakura, A. Heya, N. Matsuo, and H. Yasuda, Jpn. J. Appl. Phys. **58**, 045501 (2019).
[39]P. A. Stolk, A. Polman, and W. C. Sinke, Phys. Rev. B **47**, 5–13 (1993).
[40]E. J. Albenze, M. O. Thompson, and P. Clancy, Phys. Rev. B **70**, 094110 (2004).
[41]C. Grigoropoulos, M. Rogers, S. H. Ko, A. A. Golovin, and B. J. Matkowsky, Phys. Rev. B **73**, 184125 (2006).
[42]S. Nagaoka, C. Tahara, and M. Ishimaru, Appl. Phys. Express **16**, 015501 (2023).
[43]M. Okugawa, R. Nakamura, M. Ishimaru, H. Yasuda, and H. Numakura, AIP Adv. **6**, 125035 (2016).
[44]H. S. Chen and D. Turnbull, J. Appl. Phys. **40**, 4214 (1969).
[45]G. A. N. Connell and W. Paul, J. Non-Crystal Solids **8–10**, 215 (1972).
[46]M. L. Rudee, Thin Solid Films **12**, 207–210 (1972).
[47]H. S. Randhawa, L. K. Malhotra, H. K. Sehgal, and K. L. Chopra, Phys. Status Solidi A **37**, 313 (1976).
[48]J. C. C. Fan and C. H. Anderson, J. Appl. Phys. **52**, 4003 (1981).
[49]E. P. Donovan, F. Spaepen, D. Turnbull, J. M. Poate, and D. C. Jacobson, J. Appl. Phys. **57**, 1795 (1985).
[50]M. Liu, L. Xu, and X. Lin, Scanning **16**, 1–5 (1994).
[51]X.-w. Du, M. Takeguchi, M. Tanaka, and K. Furuya, Appl. Phys. Lett. **82**, 1108 (2003).
[52]D. G. Cahill and R. O. Pohl, Phys. Rev. B **37**, 8773 (1988).